

Langmuir Turbulence in the Arctic Ocean: Insights From a Coupled Sea Ice –Wave Model

Aikaterini Tavri¹, Chris Horvat¹, Brodie Pearson², Guillaume Boutin³, Anne Hansen², and Ara Lee²

¹Brown University, Providence, RI, USA

²Oregon State University, Corvallis, OR, USA

³Nansen Environmental and Remote Sensing Center and Bjerknes Centre for Climate Research, Bergen, Norway

Correspondence: Aikaterini Tavri aikaterini_tavri@brown.edu

Abstract. Upper-ocean mixing regulates the vertical transport of heat, momentum, and tracers in the ocean surface boundary layer. Langmuir turbulence (LT), generated by the interaction of wind stress and wave-induced Stokes drift, is a dominant mixing mechanism in the open ocean. Observations of LT in leads, polynyas, and the marginal ice zone (MIZ) confirm its presence in ice-covered regions, but its Arctic-wide occurrence and modulation by sea ice and waves remain limited in characterization. Here we present the first pan-Arctic assessment of LT mixing potential using a coupled sea ice–wave model integrating *neXtSIM* and *WAVEWATCH III*. Using wind–wave forcing metrics, we show that LT-relevant forcing beneath sea ice is spatially confined and highly intermittent. Conditions favorable for LT largely occur within the seasonal MIZ and arise episodically. Sea ice concentration sets the mean balance between wave- and shear-driven turbulence, but does not uniquely determine LT variability. The realization of wave-driven mixing depends on wave conditions and ice structure, while wind–wave misalignment plays a secondary role. As a result, LT in the Arctic MIZ typically occurs within mixed-forcing regimes, where wave-driven and shear-driven processes coexist. Our findings highlight the importance of wave–ice interactions and intermittency in shaping upper-ocean mixing under partial ice cover.

1 Introduction

The Arctic Ocean has traditionally been considered a region of weak upper-ocean mixing, primarily due to extensive sea ice cover that insulates the ocean from atmospheric forcing and dissipates wave energy (Morison et al., 1985; Pinkel, 2005). Under these conditions, turbulent exchange in the ocean surface boundary layer (OSBL) remains strongly suppressed, and vertical mixing occurs only during sporadic shear-driven and convective events. In recent decades, the rapid decline in the Arctic sea ice, marked by the loss of multiyear ice, earlier seasonal melt onset, and expansion of open water area, has increasingly exposed the Arctic Ocean to wind and wave forcing, fundamentally shifting the traditional view (Stopa et al., 2016; Armitage et al., 2017; Muilwijk et al., 2024). These changes have amplified air–sea momentum transfer (Rainville et al., 2011; Dosser and Rainville, 2016) and expanded the Marginal Ice Zone (MIZ), a transitional region characterized by discontinuous ice cover that enables surface wave propagation and interaction with the floe field (Collins et al., 2018; Boutin et al., 2020).

Within the MIZ, surface gravity waves play a central role in mediating air–sea interaction. They modulate sea ice breakup and accelerate melt through enhanced mechanical stress and turbulent mixing (Thomson and Rogers, 2014; Thomson, 2022).

25 Beyond direct wave breaking, surface waves also enhance upper-ocean turbulence through Langmuir turbulence (LT), that develops when wind-forced shear aligns with wave-induced Stokes drift (Craik and Leibovich, 1976; Leibovich, 1983; McWilliams et al., 1997). LT forms coherent, counter-rotating Langmuir cells that vertically redistribute heat, momentum, and tracers, (Skylingstad and Denbo, 1995; Kukulka et al., 2013; D’Asaro, 2014; Gargett and Grosch, 2014), and it has emerged as a key regulator of mixed layer dynamics in the open ocean (Polton and Belcher, 2007; Belcher et al., 2012; Yang et al., 2014; 30 Pearson et al., 2015). *In situ* observations show that waves can propagate long distances beneath sea ice and influence mixing near leads, polynyas, and the MIZ (Drucker et al., 2003; Kirillov et al., 2013; Horvat et al., 2020; Cooper et al., 2022). The presence of Langmuir cells in ice openings further confirms that LT remains active in ice-covered waters, albeit intermittently and with modified structure (Dethleff and Kempema, 2007; Voermans et al., 2019). Prior studies of wave–ice interactions have largely focused on mechanical processes such as ice breakup and wave attenuation (Collins et al., 2018; Squire, 2018), while 35 the role of LT in modulating turbulent mixing under sea ice remains understudied.

Experiments using ocean general circulation models, show that neglecting LT leads to systematic biases in upper-ocean structure, including underestimation of summer mixed layer depth (MLD) and misrepresentation of seasonal stratification (Li et al., 2019). Incorporating LT reduces these biases and improves simulations of sea surface temperature and ocean heat content (Fan and Griffies, 2014; Ali et al., 2019). Additionally, Large-eddy simulation (LES) studies have demonstrated that LT 40 substantially enhances upper-ocean mixing, deepening the mixed layer and increasing vertical entrainment fluxes by up to an order of magnitude relative to shear-driven turbulence alone, with more moderate increases in momentum fluxes (McWilliams et al., 1997; Sullivan et al., 2007). Therefore, representing open-ocean LT in large-scale models is essential, as it leads to significant regional and global climate impacts (Li et al., 2016, 2017). Typically, LT parameterizations are incorporated into ocean models through modifications to turbulence closure schemes such as the K-profile parameterization (KPP) (Li and Fox- 45 Kemper, 2017), enhancing upper-ocean mixing by increasing turbulent velocity scales and promoting entrainment at the base of the mixed layer (Van Roekel et al., 2012; Harcourt, 2015; Reichl et al., 2016; Li and Fox-Kemper, 2017; Pearson et al., 2019; Reichl and Li, 2019). These improve the representation of upper ocean physics but differ in their ability to represent LT across dynamical regimes, highlighting uncertainties in their formulation and performance (Li et al., 2019; Ali et al., 2019).

Despite the demonstrated importance of LT in the open ocean, these parameterizations have not been systematically evaluated 50 in ice-covered regions, where the physical environment deviates substantially from typical open-ocean conditions. In the Arctic, sea ice modifies upper-ocean mixing by limiting wave fetch, altering the directional distribution of wave energy, and preferentially attenuating short-wavelength components, thereby reducing both the magnitude and vertical extent of Stokes drift (Arduin et al., 2016, 2020; Li and Fox-Kemper, 2017). At the same time, ice motion and floe interactions introduce additional sources of shear and turbulence (Skylingstad and Denbo, 2001). Recent modeling studies have begun to explore 55 wave–ice interactions and localized mixing processes (Horvat et al., 2016; Manucharyan and Thompson, 2017; Cooper et al., 2022; Brenner and Horvat, 2024; Lo Piccolo et al., 2024). However, to our knowledge, no study has yet conducted a basin-wide, systematic evaluation of LT-driven mixing potential under realistic Arctic sea ice and wave conditions.

In this study, we use a coupled sea ice - wave model that combines the neXtSIM Lagrangian sea ice model (Rampal et al., 2016) with the WAVEWATCH III (WW3) spectral wave model (Tolman et al., 2009). This modeling framework resolves

60 surface Stokes drift, wave energy, and wind stress under evolving sea ice conditions. Using this information, we conduct an Arctic-wide assessment of LT mixing potential under realistic wave - sea ice interaction. *LT mixing potential* is defined as the amplitude of Langmuir forcing inferred from surface shear (friction velocity, u_*) and surface wave-induced Stokes drift at the surface ($u_{s(0)}$), independent of the resulting oceanic response. Our primary objective is to identify when and where conditions favorable for LT mixing emerge and persist in the Arctic in relation to seasonal sea ice advance and retreat. We evaluate the applicability of open-ocean LT parameterizations in ice-covered regions, assessing their sensitivity to sea ice conditions. In particular, we examine how wind-wave misalignment, sea ice concentration, and seasonal evolution modulate LT forcing, and whether projected LT metrics are more sensitive to environmental forcing controlling mixing. Through this analysis, we aim to provide process-based constraints on LT parameterizations in the Arctic, where wave-ice interactions fundamentally alter the structure and efficiency of upper-ocean mixing. Section 2 details the coupled model configuration, the formulation of LT-relevant parameters, and the model inputs underpinning the LT metrics. Section 3 begins with an assessment of LT-relevant wind and wave forcing in sea ice. We then characterize the spatial and temporal organization of upper-ocean mixing across the Arctic, followed by an analysis of seasonal and regional patterns in mechanically forced dissipation and the mixed-layer-averaged vertical velocity variance. Finally, we examine the influence of wind-wave misalignment on LT energetics and mixing. Section 4 discusses the implications of these findings for Arctic mixed layer dynamics and model development, and outlines key limitations of the study.

2 Data and Methods

2.1 The neXtSIM- WAVEWATCH III coupled model

We use a coupled sea ice-wave modeling framework that integrates the Lagrangian neXt-generation Sea Ice Model (neXtSIM) with the WAVEWATCH III (WW3) spectral wave model through the OASIS-MCT coupler (Boutin et al., 2021). NeXtSIM provides evolving sea ice concentration, thickness, and floe-size distribution (FSD), which govern wave attenuation and the directional filtering of wave energy. Unlike Eulerian models, neXtSIM employs a moving triangular mesh that undergoes periodic local remeshing to maintain a nominal resolution equivalent to the 25 km stereographic grid used by WW3. The two components operate on different grids, with fields exchanged every 30 minutes via interpolation onto the WW3 exchange grid. NeXtSIM is forced by the European Centre for Medium-Range Weather Forecasts (ECMWF) fifth generation reanalysis (ERA5) atmospheric fields and the GLORYS12V1 ocean reanalysis, and does not impose lateral boundary conditions for sea ice. Instead, sea ice drifts freely across open boundaries, with inflowing ice assumed to have properties consistent with the adjacent interior ice (Ólason et al., 2025). WW3 simulates wave propagation and attenuation in sea ice using the IS2+IC2 attenuation scheme, which accounts for scattering, inelastic flexure, and under-ice friction (Boutin et al., 2018). The southern boundary of the regional WW3 domain is located at 54°N, where lateral wave spectra are prescribed using the Ifremer global WW3 Modélisation et Analyse pour le Recherche Côtière (MARC) hindcast. WW3 is forced with the same ERA5 winds as neXtSIM and does not include ocean currents, neglecting wave-current interactions. This configuration reproduces realistic

wave–ice interactions in the Barents and Beaufort Seas (Ardhuin et al., 2018) and yields MIZ extents consistent with ICESat-2 observations (Boutin et al., 2022).

Simulations cover the pan-Arctic domain for 2018–2022, with three-hourly output from the coupled system. At 25km grid resolution, the marginal ice is represented as a mesoscale transition zone, without resolving individual floes and small leads. Model configuration follows Boutin et al. (2022) and table S1 lists all model variables used in this study. The framework does not include a prognostic ocean mixed layer, so surface waves do not feed back on stratification or turbulence. Ocean stratification and MLD are prescribed from GLORYS12V1 reanalysis. Langmuir-related metrics presented here represent the potential for mechanically forced mixing inferred from surface forcing and do not capture the fully realized ocean response.

The coupled framework provides key advantages over approaches that combine sea ice fields with externally derived wave products or empirical Stokes drift formulations (Webb and Fox-Kemper, 2011). In neXtSIM–WW3, Stokes drift and wave radiation stress are computed directly from the ice-attenuated wave spectrum, while the prognostic floe-size distribution modulates wave attenuation in a physically consistent manner. In contrast, ERA5 treats sea ice as land above a concentration threshold and cannot represent wave attenuation, directional filtering, or their influence on Stokes drift. These processes are essential for capturing LT forcing in dynamic sea ice conditions, and for capturing how wave–ice interactions modify Lagrangian shear relevant to LT parameterizations.

2.2 Evaluation of model inputs relevant to LT metrics

To assess the fidelity of the neXtSIM–WW3 inputs most relevant for LT diagnostics, we evaluate the surface winds, surface shear, Stokes drift, and the representation of heterogeneous sea ice and MIZ conditions. ERA5 winds, which force both neXtSIM and WW3, show increased uncertainty under strong wind and high-latitude conditions, particularly near sharp ice–open-water transitions. Consistent with this, comparison against Cross-Calibrated Multi-Platform (CCMP) v3.1 data shows that ERA5 winds are systematically weaker than satellite-derived winds, and that this bias propagates directly into the diagnosed friction velocity u_* . Over 2018–2022, area-weighted Arctic mean 10-m winds shows a mean bias of -1.46 m s^{-1} (ERA5–CCMP), an RMSE of 1.47 m s^{-1} , and a correlation of 0.99 (Fig. S1), indicating high fidelity in synoptic variability despite a low mean state bias. Because CCMP assimilates ERA5 as a background field, this comparison primarily constrains mean state uncertainty.

The fidelity of neXtSIM sea ice concentration, ice-edge location, and deformation has been demonstrated in multiple studies. Ólason et al. (2025) report pan-Arctic sea ice extent RMSE of $0.76 \times 10^6\text{ km}^2$ and show that neXtSIM reproduces observed patterns of ice drift and deformation from OSI-SAF products, supporting its ability to represent heterogeneous ice fields that modulate wave penetration and Stokes drift pathways. Accurate estimation of Stokes drift $u_{s(0)}$ further depends on realistic representation of short-wave attenuation in ice. The IS2+IC2 attenuation scheme implemented in WW3 has been shown to reproduce observed wave decay and spectral evolution in the Beaufort MIZ (Ardhuin et al., 2018), and to yield realistic pan-Arctic MIZ extents and wave-affected ice regimes consistent with ICESat-2–derived freeboard variability and floe-scale ice properties (Boutin et al., 2022). Based on sensitivity analyses and independent observational constraints, prior studies indicate that residual uncertainty in the short-wave spectrum, and hence in inferred Stokes drift, is dominated by uncertainties in wind

forcing and sea ice concentration, with magnitude on the order of tens of percent rather than order-unity errors (Ardhuin et al., 2018; Boutin et al., 2022).

2.3 Surface stress partitioning and wind–wave forcing

To characterize momentum input into the ocean mixed layer under partial ice cover, we compute an effective surface stress that partitions momentum between the ice–ocean and atmosphere–ocean interfaces. Following the framework of Brenner et al. (2021), the net ocean surface stress is defined as an area-weighted combination of ice–ocean and atmosphere–ocean stresses, scaled by the local sea ice concentration:

$$\boldsymbol{\tau}_{ocn} = A \boldsymbol{\tau}_{io} + (1 - A) \boldsymbol{\tau}_{ao} \quad (1)$$

where A is the sea ice concentration (0 = open ocean, 1 = fully ice covered), and the direct atmosphere–ocean stress is given by:

$$\boldsymbol{\tau}_{ao} = \rho_a C_{ao} |\mathbf{u}_a| \mathbf{u}_a \quad (2)$$

with ρ_a as air density, \mathbf{u}_a the 10-m wind velocity, and C_{ao} the air–sea drag coefficient over open water. Subsequently, we define an effective water-side friction velocity u_* , which represents the shear strength associated with the net surface stress transmitted to the ocean under partial ice cover:

$$u_* = \sqrt{\frac{|\boldsymbol{\tau}_{ocn}|}{\rho_o}}. \quad (3)$$

where ρ_o is the density of seawater. It provides the fundamental scaling for wind-driven mixing processes. The net surface stress $\boldsymbol{\tau}_{ao}$ represents an upper bound on the momentum flux available to drive mixed-layer shear during periods of active wave growth. This primarily affects the absolute magnitude of the diagnosed friction velocity u_* , while its spatial structure and relative variability remain more robust.

In addition to wind shear, surface waves modify upper-ocean momentum through Stokes drift, the net Lagrangian transport of water particles arising from wave orbital motion. In WW3, the surface Stokes drift components ($z = 0$) are computed from the two-dimensional wave energy spectrum $F(k, \theta)$ as:

$$U_{sx}^{z=0} = g \int \int \frac{k^2 \cos(\theta)}{\sigma^2} F(k, \theta) d\theta dk, \quad (4)$$

and

$$U_{sy}^{z=0} = g \int \int \frac{k^2 \sin(\theta)}{\sigma^2} F(k, \theta) d\theta dk. \quad (5)$$

Here, σ is the wave frequency, k is the wave number and θ the propagation direction. These expressions define the eastward and northward components of the surface Stokes drift vector u_s . The effective friction velocity and surface Stokes drift together characterize the surface shear and wave forcing that govern the mixing potential for LT under varying sea ice conditions.

2.4 Langmuir turbulence metrics in the Arctic

155 The Langmuir number (La_t) is a widely used parameter for quantifying the relative contributions of wind stress and wave-induced Stokes drift to upper ocean turbulence (McWilliams et al., 1997). It is defined as:

$$La_t = \sqrt{\frac{u_*}{u_{s(0)}}}, \quad (6)$$

where u_* is the friction velocity associated with the effective surface stress applied to the ocean, and $u_{s(0)}$ is the surface Stokes drift magnitude. In the open ocean, typical values of La_t range between 0.2 and 0.5 (Belcher et al., 2012), suggesting
 160 strong wave influence and active Langmuir circulation development, although La_t can reach values near or above 1 when wave effects are weak and wind-driven processes dominate (McWilliams et al., 1997; Belcher et al., 2012). These ranges are consistent with results from LES and field observations showing that stronger LT and deeper mixing are associated with lower La_t (Harcourt and D'Asaro, 2008). La_t is used in ocean modeling as a diagnostic of upper-ocean mixing regimes and to inform turbulence parameterizations. However, the traditional formulation implicitly assumes that the wind stress and Stokes drift are
 165 aligned. In realistic wave fields, especially in the Arctic, where mixed swell, turning winds, and ice-induced attenuation are common, misalignment can strongly reduce the effective Stokes shear that drives Langmuir circulations (Kukulka et al., 2010; Van Roekel et al., 2012; Li and Fox-Kemper, 2017).

To account for wind–wave misalignment, we adopt the *projected* Langmuir number of Van Roekel et al. (2012), which incorporates the dynamic orientation of the dominant Langmuir cells. In this framework, Langmuir cells do not necessarily
 170 align with the wind, but with the direction of maximum Lagrangian shear, set by a balance between Eulerian shear, Stokes drift, stratification, and Coriolis rotation. The orientation angle α_L represents the direction of the dominant Langmuir cells relative to the wind. Incorporating this angle yields the generalized projected Langmuir number:

$$La_{\text{proj}} \equiv \left(\frac{|u_*| \cos(\alpha_L)}{|u_{s(0)}| \cos(\theta_{ww} - \alpha_L)} \right)^{1/2}, \quad (7)$$

where θ_{ww} is the angle between the wind stress and Stokes drift vectors.

175 The Langmuir cell orientation α_L depends on the vertical structure of Lagrangian shear and cannot be directly evaluated from surface forcing alone. We use the bulk approximation α_{LOW} proposed by Van Roekel et al. (2012), which provides an *a priori* estimate of the cell orientation based on depth-averaged Lagrangian shear. This estimate assumes that the Eulerian shear follows a law-of-the-wall profile, that cross-wind shear is negligible, and that Stokes shear is known from wave fields. The Lagrangian shear is expressed as the sum of Eulerian and Stokes contributions, with the Eulerian shear represented using
 180 a law-of-the-wall profile:

$$\tan \alpha_{\text{LOW}} \approx \frac{\langle \partial v_s / \partial z \rangle_{D_L}}{\langle -u_* / (\kappa z) + \partial u_s / \partial z \rangle_{D_L}}, \quad (8)$$

where angle brackets denote a depth average over the Langmuir-affected layer D_L , and κ is the von Kármán constant. This approximation provides a practical estimate of Langmuir cell orientation across a range of wind–wave misalignment conditions in LES, although it remains an idealized representation (Van Roekel et al., 2012).

185 2.4.1 Surface forcing metrics and mixing regime classification

We introduce two complementary metrics to evaluate the LT mixing potential under partial sea ice cover. The first evaluates how frequently surface forcing beneath sea ice resembles open-water conditions, based on exceedance metrics for surface stress and wave forcing. The second classifies near-surface ocean conditions into discrete mixing regimes based on the Langmuir number La_t and tracks transitions between these regimes over space and time.

190 We define exceedance metrics to quantify how often the near-surface wind and wave forcing in ice-covered regions approaches values typical of the ones in open ocean. The two primary LT drivers considered are the surface friction velocity (u_*) and the surface Stokes drift velocity ($u_{s(0)}$). For each season (s) and grid cell (x, y), we define an open-water (OW) benchmark by computing the median value of a given variable X over all ice-free conditions ($SIC < 0.15$):

$$X_{\text{OW}}^{(s)} = \text{median}\{X_t(x, y) : SIC_t(x, y) < 0.15, t \in s\}. \quad (9)$$

195 This benchmark represents the typical magnitude of atmosphere-ocean or wave-induced surface forcing under ice-free conditions during a given season.

At each ice-covered grid cell ($SIC \geq 0.15$), we compute the fraction of time steps for which the local value exceeds the seasonal OW benchmark. For a single variable, the exceedance metric is defined as

$$\text{Exceedance}_X^{(s)}(x, y) = \frac{N_t \left[SIC_t(x, y) \geq 0.15 \wedge X_t(x, y) \geq X_{\text{OW}}^{(s)} \right]}{N_t [SIC_t(x, y) \geq 0.15]}, \quad (10)$$

200 where $N_t[\cdot]$ denotes the number of seasonal time steps satisfying the specified condition. Seasons follow meteorological definitions: winter (DJF), spring (MAM), summer (JJA), and fall (SON). Grid cells are defined on a stereographic grid with approximately uniform spacing (25 km), such that their areas are effectively equal and statistics based on grid cell counts approximate area-weighted statistics.

To isolate conditions most relevant for LT, we further define a joint exceedance metric that quantifies the fraction of ice-
205 covered time during which both surface friction velocity and surface Stokes drift simultaneously exceed their respective OW seasonal medians:

$$\text{JointExceedance}^{(s)}(x, y) = \frac{N_t \left[SIC_t(x, y) \geq 0.15 \wedge u_{*,t}(x, y) \geq u_{*,\text{OW}}^{(s)} \wedge u_{s(0),t}(x, y) \geq u_{s(0),\text{OW}}^{(s)} \right]}{N_t [SIC_t(x, y) \geq 0.15]}. \quad (11)$$

These exceedance metrics provide a physically interpretable measure of the frequency and persistence of LT-relevant surface forcing in ice-covered regions, relative to open-ocean benchmarks. As the OW benchmark varies seasonally, exceedance reflects
210 relative forcing intensity and should be interpreted in the context of seasonal variability in OW conditions.

To characterize the evolving balance between wind- and wave-driven mixing, we classify surface forcing into three regimes using the turbulent Langmuir number La_t (Li et al., 2019). This classification represents a reduced, one-dimensional approximation of LES-based regime diagrams, which are formally defined in terms of both La_t and a stability parameter h/L_L , where h is the MLD and L_L is a Langmuir stability length scale that incorporates buoyancy forcing. Because our framework does

215 not explicitly resolve buoyancy forcing or prognostic mixed layer dynamics, we collapse this two-parameter space onto La_t alone and adopt representative thresholds to distinguish wave-dominated, shear-dominated, and intermediate mixed-forcing conditions. At each time step T and grid cell (x, y) , the regime is defined as:

$$\mathcal{R}(x, y, T) = \begin{cases} 1 & \text{if } La_t(x, y, T) > 0.94 \quad (\text{Shear-dominated}) \\ 2 & \text{if } 0.43 < La_t(x, y, T) \leq 0.94 \quad (\text{Mixed-forcing}) \\ 3 & \text{if } La_t(x, y, T) \leq 0.43 \quad (\text{Wave-dominated}). \end{cases} \quad (12)$$

To relate mixing regimes to sea ice conditions, we define spatial regions $\Omega(T)$ at each time step based on the local sea ice

$$\begin{aligned} \Omega_{\text{ice}}(T) &= \{(x, y) \mid \text{SIC}(x, y, T) > 0.8\}, \\ 220 \quad \Omega_{\text{MIZ}}(T) &= \{(x, y) \mid 0.15 \leq \text{SIC}(x, y, T) \leq 0.8\}, \\ \Omega_{\text{OW}}(T) &= \{(x, y) \mid \text{SIC}(x, y, T) < 0.15\}. \end{aligned} \quad (13)$$

For each region Ω and regime $r \in \{1, 2, 3\}$, we compute the spatial fraction of grid cells occupying regime r at time T as

$$f_r^\Omega(T) = \frac{1}{|\Omega(T)|} \sum_{(x, y) \in \Omega(T)} \delta(\mathcal{R}(x, y, T) = r), \quad (14)$$

where $\delta(\cdot)$ is the indicator function and $|\Omega(T)|$ is the number of valid grid cells in region $\Omega(T)$.

Beyond regime occupancy, we assess the temporal stability of the surface forcing balance by tracking transitions between regimes. For each grid cell (x, y) , we count transitions from regime r_n to r_m between successive time steps, restricted to 225 periods when the grid cell remains within the same ice regime Ω :

$$T_{r_n \rightarrow r_m}^\Omega(x, y) = \sum_{T=2}^{T_{\text{max}}} \delta(\mathcal{R}(x, y, T-1) = r_n) \delta(\mathcal{R}(x, y, T) = r_m) \delta((x, y) \in \Omega(T-1) \cap \Omega(T)). \quad (15)$$

Spatial differences in temporal sampling are evaluated using transition counts, normalized by the number of time steps a grid cell resides within region Ω ,

$$230 \quad \bar{T}_{r_n \rightarrow r_m}^\Omega(x, y) = \frac{T_{r_n \rightarrow r_m}^\Omega(x, y)}{N_\Omega(x, y)}, \quad (16)$$

where $N_\Omega(x, y)$ denotes the total number of time steps satisfying the regional criterion. The resulting normalized transition frequency provides a measure of how often the dominant surface forcing balance reorganizes at a given location over the analysis period.

2.4.2 Langmuir Turbulence Energetics

235 To examine how LT modifies upper-ocean energetics, we evaluate two complementary metrics based on the vertically integrated turbulent kinetic energy (TKE) budget: (i) the mixed-layer-averaged vertical velocity variance, $\langle w'^2 \rangle_{H_{ML}}$, and (ii) the mechanically driven dissipation rate, $\varepsilon_{\text{mech}}$. Both are derived from empirically based LES scalings and provide complementary diagnostics of turbulence intensity and energy dissipation.

We compute $\langle w'^2 \rangle_{H_{ML}}$ following the LES-based scaling of Van Roekel et al. (2012):

$$240 \quad \langle w'^2 \rangle_{H_{ML}} = 0.6 [u_* \cos(\alpha_{LOW})]^2 (1 + (c_1 La_x)^{-2} + (c_2 La_x)^{-4}), \quad (17)$$

where u_* is the friction velocity and La_x denotes the Langmuir number metric used in the scaling. The La_x^{-2} and La_x^{-4} terms capture the nonlinear enhancement of vertical velocity variance by Langmuir forcing, with lower Langmuir numbers indicating stronger turbulence. The projection factor $\cos(\alpha_{LOW})$ accounts for the orientation of Langmuir cells relative to the wind. For the wind-aligned case, we set $La_x = La_t$ and $\alpha_{LOW} = 0$, while for the projected formulation we use $La_x = La_{proj}$. We adopt
 245 $(c_1, c_2) = (3.1, 5.7)$ for La_t and $(c_1, c_2) = (3.1, 5.4)$ for La_{proj} , consistent with the original LES fits following Van Roekel et al. (2012). Because this scaling is derived under weak or destabilizing buoyancy forcing, the resulting values of $\langle w'^2 \rangle_{H_{ML}}$ are interpreted as a measure of LT mixing potential rather than a direct prediction of the realized turbulent state.

The contribution of LT to upper-ocean energy dissipation is estimated using a reduced form of the scaling framework of Belcher et al. (2012). In the mixed-layer interior, turbulent dissipation can be approximated as the sum of contributions from
 250 shear, Stokes drift, and buoyancy forcing. Factoring out the shear-based velocity scale yields:

$$\varepsilon \sim \frac{u_*^3}{H_{ML}} \left[A_s + A_L La_x^{-2} + A_c \frac{B_s H_{ML}}{u_*^3} \right], \quad (18)$$

where H_{ML} is the mixed-layer depth, La_x characterizes the relative importance of wave forcing, and B_s is the surface buoyancy flux. The coefficients A_s , A_L , and A_c are empirical constants of order unity representing shear-, Langmuir-, and buoyancy-driven contributions, respectively. The Langmuir contribution scales as La_x^{-2} , consistent with the ratio of Stokes drift to friction
 255 velocity and with LES results showing enhanced mixing under strong wind-wave coupling.

Consistent with the surface-forcing-only framework described in Section 2.1, we omit the buoyancy contribution in Eq. (19) and adopt a reduced formulation that isolates mechanically driven turbulence:

$$\varepsilon_{\text{mech}} = \frac{u_*^3}{H_{ML}} (1 + \beta, La_x^{-2}), \quad (19)$$

where the second term represents enhancement of dissipation by wave-induced Stokes drift. The empirical coefficient β
 260 parameterizes the efficiency of this enhancement, with LES suggesting $\beta \approx 0.15$ under weakly stratified conditions. The resulting $\varepsilon_{\text{mech}}$ is used here as a diagnostic of mechanically mediated energy input associated with wind-wave forcing and is interpreted as a proxy for LT-driven mixing potential.

The mixed-layer depth H_{ML} is taken from the GLORYS12 reanalysis, which provides a spatially and seasonally varying vertical scale for interpreting mechanically forced turbulence. Although GLORYS12 does not explicitly resolve ice-modified
 265 boundary-layer processes, it offers a physically consistent bulk estimate of the mixed-layer depth suitable for vertically integrated diagnostics.

All spatial statistics are computed on the model exchange grid, which has an approximately uniform 25 km resolution in the polar stereographic projection. Grid cell area varies slightly with latitude, but cosine-latitude weighting yields negligible differences, indicating that grid-cell-based statistics are representative of area-weighted behavior.

3.1 Spatiotemporal variability of surface forcing across the Arctic

Figure 1 summarizes the seasonal variability of surface forcing through open-water (OW) exceedance of friction velocity (u_*), Stokes drift ($u_{s(0)}$), and their joint occurrence (see Eqs. 10–11). The top panels show probability density functions (PDFs) of exceedance fractions across all ice-covered grid cells ($SIC \geq 0.15$), and the bottom panels map the spatial distribution of joint exceedance relative to seasonal median sea ice concentration (SIC) contours. The PDFs (Fig. 1a–c) reveal an asymmetry between atmospheric and wave forcing. Exceedance of wind stress (u_*) spans a broad range across all seasons, indicating that atmospheric forcing in ice-covered regions frequently reaches magnitudes comparable to OW conditions. In contrast, Stokes drift ($u_{s(0)}$) exceedance is strongly skewed toward low values, with a rapid decay toward higher exceedance fractions, reflecting the attenuation of wave energy within ice-covered regions (Liu and Mollo-Christensen, 1988; Arduin et al., 2016; Herman, 2017). As a result, joint exceedance closely follows the Stokes drift distribution, highlighting the dominant role of wave forcing in setting LT-relevant mixing conditions.

Spatially (Fig. 1d–g), joint exceedance is concentrated along the MIZ, closely aligned with the 15–80% SIC contours. The highest occurrence is found in the Barents, Greenland, and Chukchi Seas, where fragmented, mobile ice reduces wave attenuation and allows intermittent penetration of wave energy into the ice-covered ocean. Because the OW benchmark is defined separately for each season, exceedance represents a measure of relative forcing intensity rather than absolute magnitude. Across all seasons, joint exceedance remains limited, rarely exceeding 0.2, indicating that simultaneous strong wind and wave forcing beneath sea ice is uncommon. Seasonal differences therefore reflect both variations in forcing and shifts in the reference state. During winter and transitional seasons (DJF, MAM, SON), exceedance is more spatially continuous along the MIZ, consistent with enhanced wave–ice interaction under storm-driven conditions. However, winter shows comparatively low exceedance despite strong winds and wave heights, because the open-water reference state is also elevated, raising the threshold for exceedance. In contrast, fall (SON) shows the highest frequency of elevated joint exceedance values, even though wave heights are more moderate than in winter (Fig. S2). This reflects the combination of a lower open-water reference and more efficient wave penetration into fragmented ice cover, allowing sea ice conditions to more frequently approach OW forcing. Summer (JJA) shows a different regime. Weaker open-water winds and waves reduce the seasonal benchmark, such that moderate forcing more readily exceeds the reference. As a result, exceedance is spatially widespread. However, the magnitude of exceedance remains low, indicating that this broad signal corresponds to weak LT-relevant forcing.

Based on the exceedance metrics, LT-relevant mixing is primarily controlled by the availability and intermittency of wave forcing. Limited wave penetration beneath sea ice suppresses Stokes drift and inhibits LT, favoring predominantly shear-driven mixing, while episodic storm-driven events in the MIZ can temporarily establish open-water-like forcing beneath the ice.

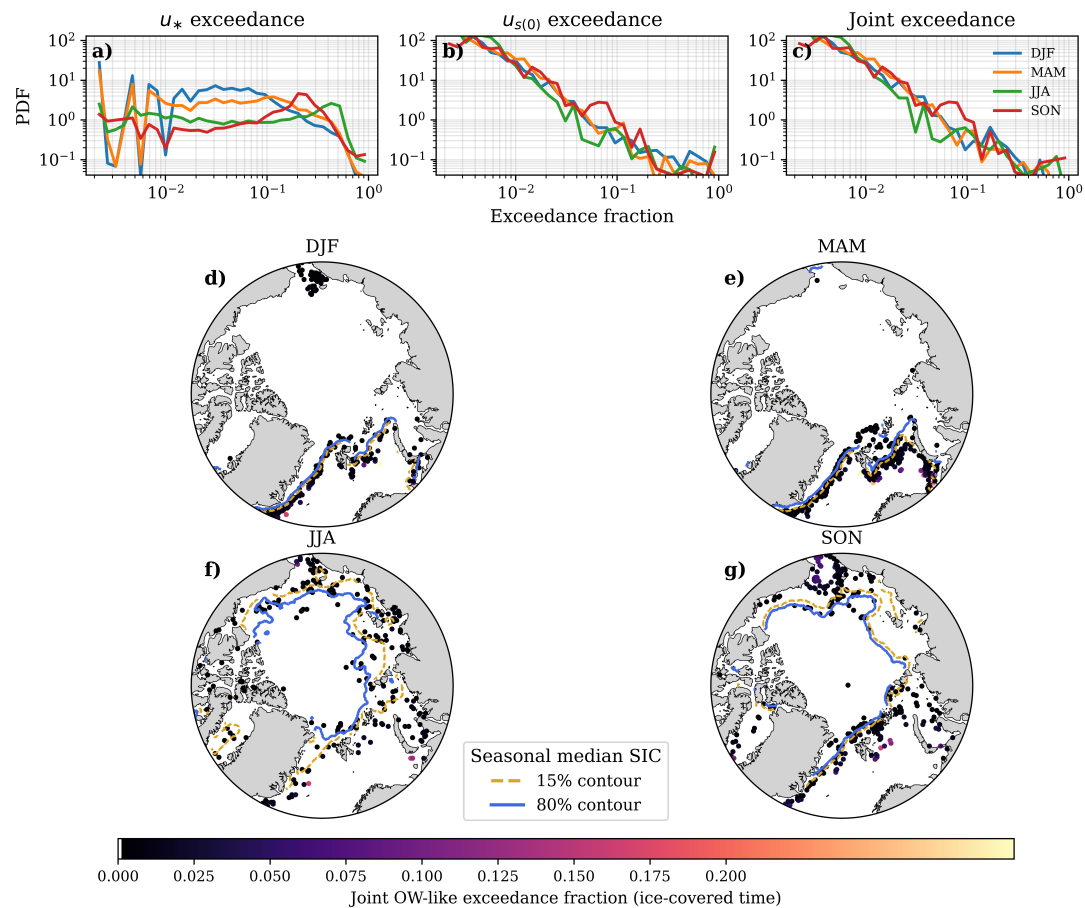


Figure 1. Seasonal exceedance of wind–wave surface forcing beneath Arctic sea ice. (a–c) Probability density functions (PDFs) of exceedance fractions for surface friction velocity (u_*), surface Stokes drift ($u_{s(0)}$), and their joint occurrence, computed over ice-covered conditions ($SIC \geq 0.15$) relative to seasonal open-water medians ($SIC < 0.15$). (d–g) Spatial distribution of the joint exceedance fraction, defined as the fraction of under-ice time during which both u_* and $u_{s(0)}$ simultaneously exceed their respective seasonal open-water medians. Elevated values (yellow–orange) indicate regions where wind and wave forcing intermittently reach open-ocean–like magnitudes despite the presence of sea ice. Dashed and solid contours denote the seasonal median **15%** (gold) and **80%** (blue) sea ice concentration boundaries, respectively, providing context for the marginal ice zone and consolidated pack ice. Joint exceedance is shown only at grid cells that experience sea ice conditions at least once during each season.

300 3.2 Mapping upper-ocean mixing regime dynamics in the Arctic

To further explore the controls on LT mixing potential, we examine the spatial and seasonal structure of the turbulent Langmuir number (La_t). All La_t medians are computed over the full spatial domain shown in Figure 2, without restricting the analysis based on sea ice concentration. The five-year climatological median (Figure 2a) reveals a persistent band of low La_t encircling the perennial ice pack and closely following the climatological 15% SIC contour and consistent with patterns shown in Figure 1. Elevated median La_t values (> 1) dominate the central Arctic under compact ice cover, indicating a shear-dominated mixing regime with limited wave influence. In contrast, moderate to low median La_t values (< 0.45), which show LT mixing potential, are confined to narrow, seasonally evolving bands along the ice edge. In OW conditions ($SIC < 0.15$), median La_t values are generally below 0.35, consistent with the range identified by Belcher et al. (2012) as favorable for LT mixing. The spatial and seasonal patterns in La_t closely reflect the exceedance statistics, reinforcing that wave-driven mixing is intermittent and strongly modulated by the sea ice cover. As ice concentration increases, wave attenuation limits Stokes-driven forcing, shifting the balance toward shear-dominated mixing and reducing LT mixing potential.

Seasonal medians (Figures 2b–e) further depict how transitions in ice state modulate the balance between wave and wind forcing. During winter and spring (Figures 2b–c), sharp gradients in La_t delineate the transition from wave-influenced conditions near the ice edge to shear-dominated regimes within the consolidated ice. Compact ice cover strongly attenuates wave energy, limiting the penetration of Stokes drift in ice-covered regions, even under periods of strong wind forcing. In contrast, summer and fall (Figures 2d–e) show a broader and more continuous band of reduced La_t extending into the seasonal sea ice zone. Lower ice concentration and increased ice mobility can reduce wave attenuation and allow wave-driven forcing to extend farther into the seasonal MIZ, even without stronger wave conditions. These patterns reinforce that departures from open-ocean La_t values are primarily associated with modulation of Stokes drift by sea ice combined with changes in wind forcing. The seasonal MIZ emerges as a distinct transition zone, where the balance between shear- and wave-driven turbulence can shift toward Langmuir-favorable conditions, while the interior pack remains persistently shear-dominated year-round.

3.3 Mapping upper-ocean mixing regime dynamics in the Arctic

Figure 3 synthesizes the spatial structure, temporal variability, and persistence of upper-ocean mixing regimes under ice-covered conditions ($SIC \geq 0.15$), based on the regime classification defined in Eq. (12) and the transition framework described in Eqs. (13–16). Panel (a) shows the dominant mixing regime at each grid cell, defined as the regime occurring for at least 50% of ice-covered time. The Arctic interior is characterized primarily by shear-driven mixing ($La_t \geq 0.94$), while mixed ($0.43 \leq La_t < 0.94$) and wave-driven ($La_t < 0.43$) regimes are confined to the seasonal MIZ and regions near the ice edge, where wind and wave forcing increasingly compete. Panel (c) maps the normalized frequency of regime transitions, expressed as the number of regime changes per ice-covered day. Enhanced regime instability is strongly localized within the MIZ, particularly along sectors exposed to episodic wave activity and intermittent OW conditions. This spatial pattern is consistent with fetch-limited wave growth in partial ice cover, where intermittent Stokes drift enhances variability in the relative balance between wind and wave forcing (Brenner and Horvat, 2024). In contrast, pack ice has uniformly low transition rates, indicating

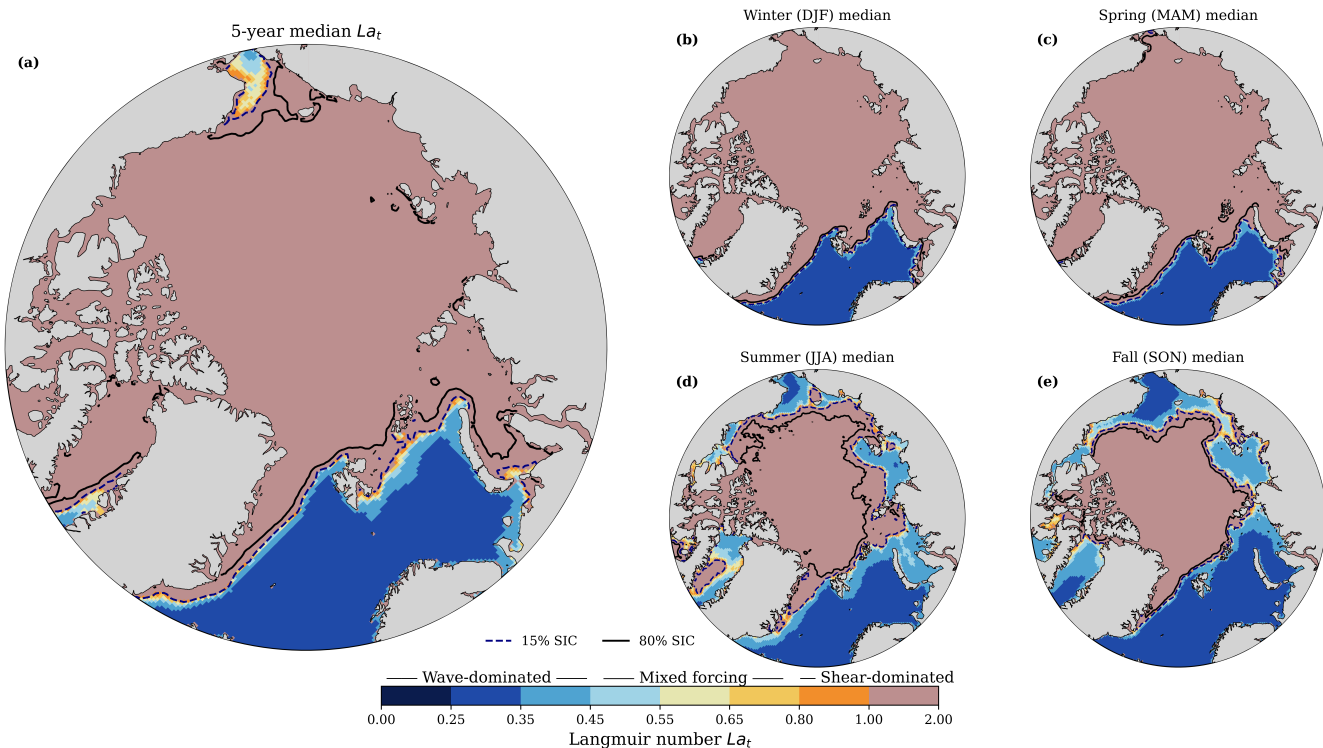


Figure 2. Spatial distribution of the median Langmuir number La_t , integrated over 2018 to 2022, along with its seasonal medians. Panel (a) shows the five-year climatological median of the Langmuir number La_t computed across all seasons. The median 15% and 80% SIC contours are overlaid in dashed dark blue and solid black lines marking the median SIC-defined extent of the MIZ across seasons. Panels (b–e) show the medians for winter (DJF), spring (MAM), summer (JJA), and fall (SON), respectively. In all panels, La_t is shown for all ocean grid cells without applying a SIC mask; SIC contours are overlaid for context.

stable and persistent forcing conditions. Localized transitions within consolidated ice likely reflect episodic openings (e.g., leads and polynyas) that temporarily allow wave generation and induce short-lived shifts in mixing regime.

335 Panels (b) and (d), restricted to MIZ grid cells ($0.15 \leq SIC \leq 0.8$), further resolve the temporal characteristics of regime variability. Regime instability (panel b), defined as the fraction of MIZ grid cells undergoing at least one transition within a 30-day window, reveals a pronounced seasonal cycle with peaks during periods of ice advance and retreat. These peaks precede maxima in MIZ area, indicating that enhanced regime variability occurs prior to, rather than as a consequence of, MIZ expansion. This behavior is consistent with wind, wave, and ice forcing becoming comparable during seasonal transitions in
 340 the MIZ, such that no single regime dominates. Small variations in forcing can shift the balance between regimes, leading to frequent transitions and elevated instability along the evolving MIZ boundary. Panel (d) relates regime instability to persistence by comparing the mean time between regime transitions with the longest continuous duration of a single regime within MIZ grid cells. Median regime persistence increases with increasing inter-transition time, although the relationship is nonlinear.

Persistence rises rapidly at short timescales before approaching a plateau at longer intervals, with the transition occurring
345 at inter-transition timescales of approximately several weeks ($\sim 20\text{--}50$ days), depending on location within the MIZ. The
broad interquartile range at short transition intervals reflects substantial variability in intermittently forced regions near the
ice edge, where regimes are frequently disrupted. In contrast, longer transition intervals correspond to more sustained and
dynamically stable regimes. Peak instability (~ 0.1 transitions per day) corresponds to approximately 2–3 transitions per month,
with mean intervals of $\sim 10\text{--}30$ days between transitions. Despite this relatively frequent switching, individual regimes persist
350 for $\sim 50\text{--}150$ days, increasing to $\sim 100\text{--}200$ days under low transition frequencies. Overall, this indicates that MIZ upper ocean
mixing is characterized by intermittent regime shifts superimposed on otherwise persistent states, rather than continuous or
rapid switching, with regime evolution occurring on sub-seasonal timescales.

Figure 4 provides complementary insight into how both local and spatially aggregated values of La_t depend on SIC, and
helps contextualize the spatial regime structure from in Figure 3. Panel (a) shows that median La_t generally increases with SIC
355 across all seasons, indicating a systematic shift toward shear-dominated mixing as ice cover increases. Conditions associated
with strong LT mixing potential ($La_t < 0.43$) are largely confined to OW or low SIC, whereas shear-dominated regimes ($La_t >$
 0.94) dominate at moderate to high SIC. This behavior is consistent with increasing attenuation of wave energy and reduced
Stokes drift under higher ice concentrations. During summer, however, the relationship deviates from this monotonic trend.
At high SIC ($\gtrsim 0.8$), median La_t decreases, indicating a relative increase in wave influence despite high ice concentration.
360 Additional diagnostics (Fig. S3) show that in this regime La_t exhibits limited dependence on sea ice thickness, but decreases
rapidly with increasing significant wave height (h_s) over the range 0–1 m. This suggests enhanced sensitivity of La_t to wave
forcing, where even modest increases in wave height can substantially increase Stokes drift and reduce La_t . This is consistent
with melt-season conditions in which the ice cover becomes mechanically weakened and increasingly spatially heterogeneous.
Partial fragmentation and floe-scale openings allow intermittent wave transmission or local, fetch-limited wave generation,
365 while spatial variability in wind stress over melting ice may reduce shear-driven turbulence. Although these processes are not
explicitly resolved at model resolution, the results indicate that wave forcing can remain dynamically relevant even at high SIC.
In this context, SIC provides a first-order constraint on mixing regimes, but does not uniquely determine the relative importance
of wave-driven turbulence during the melt season.

Panel (b) highlights the role of local spatial variability by showing the distribution of La_t within 3×3 grid-cell neighborhoods.
370 The distributions of La_t^{\min} , La_t^{mean} , and La_t^{\max} demonstrate that a wide range of mixing states can coexist locally, even under
similar SIC conditions. In particular, La_t^{\min} captures the most wave-influenced conditions within a neighborhood, while La_t^{\max}
reflects the most shear-dominated state. The large spread between these values indicates strong heterogeneity in wave and
shear forcing, consistent with a dynamic ice cover containing a mixture of wave-active and wave-suppressed regions. Panel (c)
further quantifies this heterogeneity as the difference between local maximum and minimum La_t within each neighborhood.
375 Heterogeneity increases from low SIC and peaks within the MIZ (SIC $\approx 0.3\text{--}0.5$), reflecting the coexistence of wave- and
shear-dominated regimes. At higher SIC, heterogeneity decreases, indicating a transition toward more spatially uniform forcing
conditions. Overall, these show that while SIC governs the large-scale transition between mixing regimes, the realized La_t

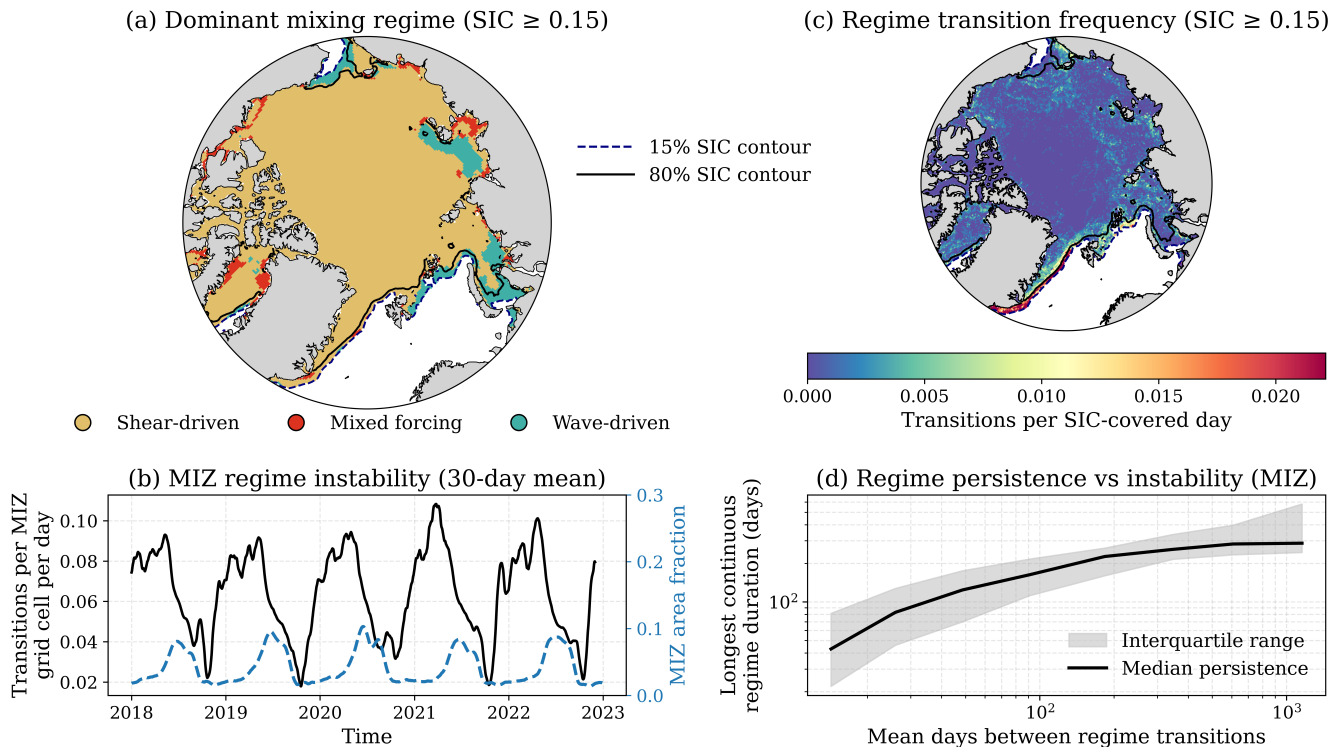


Figure 3. Spatial and temporal characteristics of upper-ocean mixing regime dynamics under sea ice for $SIC \geq 0.15$. (a) Dominant mixing regime defined as the regime occupying at least 50% of SIC-covered days at each grid cell over the analysis period. Shear-driven conditions dominate the compact ice interior, while mixed and wave-driven regimes preferentially occur near the ice edge and in seasonally ice-covered regions. Dashed and solid contours indicate the 15% and 80% sea ice concentration (SIC) thresholds, respectively. (b) Time series of marginal ice zone (MIZ; $0.15 \leq SIC \leq 0.8$) regime instability, defined as the fraction of MIZ grid cells undergoing at least one regime transition within a 30-day window (black), together with the contemporaneous fraction of the Arctic domain classified as MIZ (blue, dashed). (c) Normalized regime transition frequency (transitions per SIC-covered day) for $SIC \geq 0.15$, highlighting enhanced temporal variability along the MIZ and reduced variability within the compact ice interior. (d) Relationship between regime persistence and instability within the MIZ, shown as the median longest continuous regime duration (black) and interquartile range (shading) binned by the mean number of days between regime transitions. Increasing transition frequency is associated with a systematic reduction in regime persistence.

within a given SIC range depends strongly on local ice structure. Fragmentation and spatial heterogeneity in sea ice conditions modulate the intermittency of wave forcing, resulting in highly variable mixing conditions.

380 3.4 Pan-Arctic dissipation rates and seasonality

Mechanically driven dissipation provides a bulk measure of wind and wave energy input to the upper ocean and complements the regime-based analysis of LT. In our framework, $\varepsilon_{\text{mech}}$ quantifies the magnitude of mechanically mediated energy input, while La_t determines how this energy is partitioned between shear- and wave-driven processes. Figure 5a shows that the

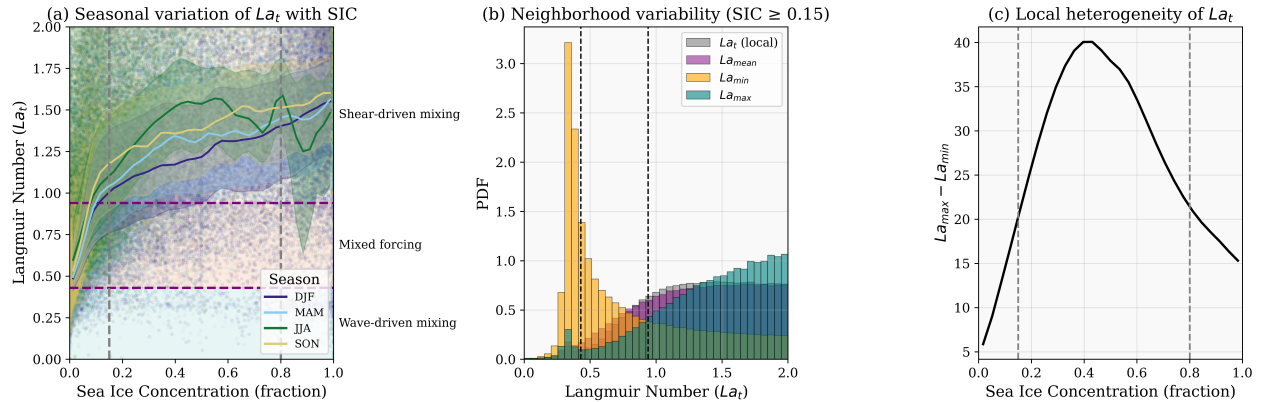


Figure 4. Langmuir number dependence on sea ice concentration and spatial variability. (a) Parametric relationship between La_t and binned sea ice concentration (SIC). Solid lines denote the seasonal median within each SIC bin, with shading indicating interquartile ranges. Purple dashed lines mark the wave-dominated ($La_t < 0.43$) and shear-dominated ($La_t > 0.94$) regime thresholds. (b) Normalized histograms of La_t computed from local grid-cell values and 3×3 neighborhood statistics (mean, minimum, and maximum), aggregated over all ice-covered grid cells ($SIC \geq 0.15$). (c) Median local heterogeneity in La_t , defined as $La_{t,max} - La_{t,min}$ within 3×3 neighborhoods, as a function of SIC.

spatial distribution of median ε_{mech} is strongly structured by surface forcing, with enhanced dissipation along the MIZ and
 385 in peripheral seas exposed to open-ocean winds and wave activity. In contrast, the central pack ice exhibits lower dissipation,
 consistent with reduced momentum transfer and attenuated wave forcing beneath consolidated ice. This pattern reflects the
 large-scale distribution of mechanically driven energy input and highlights regions where wind-wave forcing recurrently
 couples to the upper ocean. Panel (b) shows dissipation intermittency, defined as $\log_{10}(P_{90}/\text{median})$ of ε_{mech} , where the
 90th percentile and median are computed from the temporal distribution at each grid cell. This metric quantifies the relative
 390 importance of extreme events compared to the background state. High intermittency is strongly localized to narrow MIZ
 regions and ice-edge corridors, indicating that dissipation in these areas is dominated by episodic events. In contrast, regions
 with elevated median dissipation but low intermittency reflect more persistent, but still moderate, energy input.

The spatial correspondence between highly intermittent dissipation and regime-transition hotspots suggests that frequent
 mixing-regime changes arise where wind-, wave-, and ice-mediated forcing alternately dominate on short timescales. This link
 395 is further supported by the Arctic-wide time series in panel (c), which shows that variability in ε_{mech} is driven by intermittent
 extremes superimposed on a low median background. The large interquartile range relative to the median indicates that rare,
 high-energy events contribute disproportionately to temporal variability. This indicates that mechanical dissipation in the Arctic
 is not controlled by the mean state, but by intermittent high-energy events that dominate variability. Panel (d) shows that
 dissipation is strongly modulated by season, with peaks in late summer and early autumn and a minimum during late winter
 400 under consolidated ice. This seasonal cycle reflects the combined influence of increasing wind stress, reduced ice cover, and

enhanced wave activity, all of which act to amplify mechanical energy input into the mixed layer. In the MIZ, mean forcing sets the spatial structure of dissipation, while intermittent events control its variability.

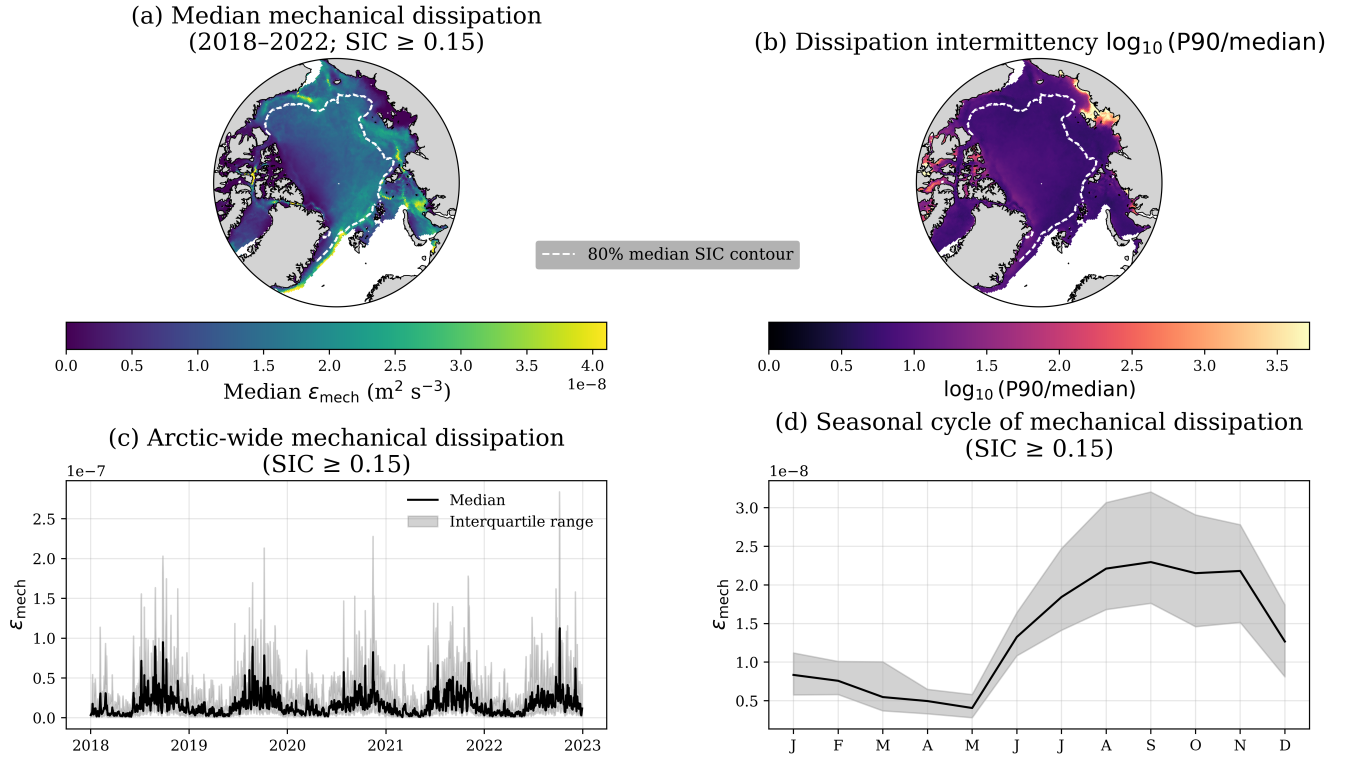


Figure 5. Mechanical dissipation magnitude and intermittency within the Arctic marginal ice zone (2018–2022). (a) Spatial distribution of the aggregated median mechanically forced dissipation, ϵ_{mech} , evaluated for ice-covered conditions (SIC ≥ 0.15). (b) Dissipation intermittency index, defined as $\log_{10}(\text{P90}/\text{median})$ of ϵ_{mech} . (c) Arctic-wide temporal evolution of mechanically forced dissipation aggregated over all grid cells classified as MIZ (SIC ≥ 0.15), shown as the spatial median (black line) with interquartile range (shading), illustrating the strongly intermittent nature of MIZ energy input. (d) Seasonal cycle of mechanically forced dissipation within the MIZ, constructed from the monthly climatology of the spatial median in panel (c), with shading indicating the interquartile range.

3.5 Impact of wind–wave misalignment on Langmuir turbulence efficiency

The contribution of wave-induced forcing to upper-ocean mixing depends not only on wave strength but also on the relative
 405 alignment between wind and waves. To quantify how directional misalignment modulates LT mixing potential, we compare
 wind-aligned and dynamically projected Langmuir metrics across the Arctic. Misalignment variability is evaluated using the
 temporal standard deviation of the log-ratio between projected and aligned Langmuir numbers, $\sigma_t[\log(La_{\text{proj}}/La_t)]$, which
 captures fluctuations in the effective projection of Stokes forcing onto the Langmuir cell axis. Pan-Arctic spatial patterns
 (Figure 6a) show that variability in the projected-to-aligned Langmuir number ratio ranges from approximately 0.05 to 0.30,

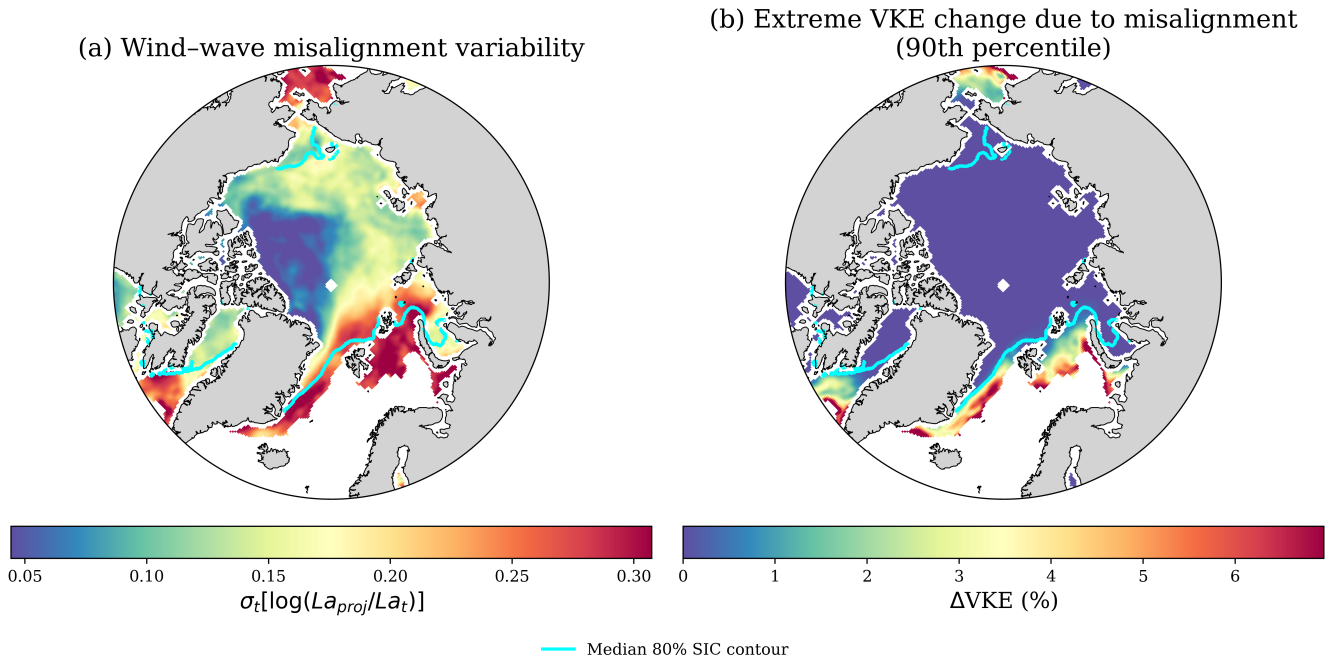


Figure 6. Impact of wind–wave misalignment on Langmuir turbulence across the Arctic. (a) Spatial variability of the projected-to-aligned Langmuir number ratio, expressed as the temporal standard deviation $\sigma_t[\log(La_{proj}/La_t)]$, showing regions where wind–wave misalignment most strongly modulates LT diagnostics. (b) Corresponding impact of misalignment on LT energetics, shown as the 90th percentile change in normalized vertical kinetic energy (ΔVKE , %), indicating the upper bound of misalignment effects. The cyan contour denotes the median 80% sea ice concentration.

410 with the largest values confined to the MIZ, particularly in regions of persistent wave–ice interaction such as the Barents and Greenland Seas. In contrast, the central Arctic exhibits consistently low variability ($\lesssim 0.1$), reflecting weak wave forcing in compact ice cover. Despite this pronounced spatial variability in diagnostic LT metrics, the impact on LT energetics is limited. The 90th percentile change in VKE (Figure 6b) remains below $\sim 1\%$ across most of the ice-covered Arctic and exceeds 4–6% only in localized regions near the ice edge. These regions correspond to partial ice cover and active wave propagation, where
 415 Stokes drift is sufficiently strong for directional effects to influence the projected shear. These magnitudes indicate that although misalignment can significantly perturb diagnostic LT metrics, its effect on the resulting mixing is comparatively weak.

To assess how frequently wind–wave misalignment occurs and how it relates to LT variability, we examine the distribution of misalignment angles together with their co-occurrence with wave forcing and the resulting LT response (Figure 7). The angle distribution (Figure 7a) shows that moderate-to-large misalignment is relatively common, with more than half of cases
 420 exceeding $\sim 30^\circ$. However, the joint distribution with wave strength (Figure 7b) indicates that these larger angles are most often associated with relatively weak wave forcing. The energetic response remains small across all angles (Figure 7c), with changes in VKE close to zero in most cases and only limited variability at larger misalignment. These suggest that variability

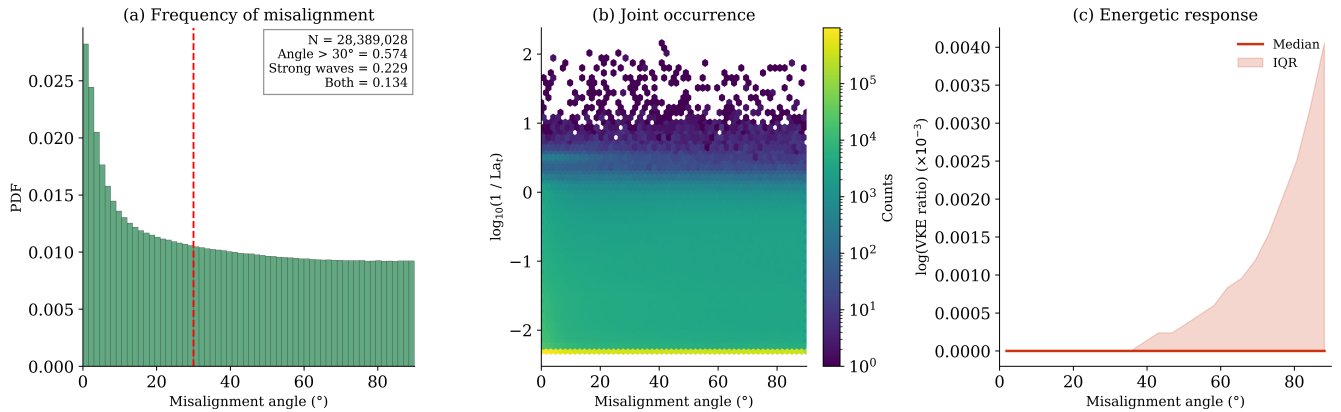


Figure 7. Frequency and impact of wind–wave misalignment on Langmuir turbulence (LT). (a) Probability density function (PDF) of wind–wave misalignment angles for all ice-covered conditions ($SIC \geq 0.15$). The dashed line indicates a threshold of 30° , used to distinguish moderate-to-large misalignment. Values inset in the panel show the fraction of samples exceeding the angle threshold, the fraction associated with relatively strong wave forcing (upper quartile of $1/La_t$), and the fraction satisfying both conditions simultaneously. (b) Joint distribution of misalignment angle and relative wave forcing, represented by $\log_{10}(1/La_t)$, with color indicating occurrence counts. (c) Energetic response to misalignment, expressed as the median log-ratio of vertical kinetic energy (VKE) computed with and without directional effects, shown as a function of misalignment angle. Shading denotes the interquartile range (IQR).

in projected LT metrics does not translate directly into changes in mixing, and that the influence of misalignment on LT is secondary compared to variations in wave forcing.

425 4 Discussion and Conclusions

We used a coupled sea ice–wave modeling framework to quantify the controls on LT mixing potential across the Arctic basin. We show that LT-relevant forcing is fundamentally wave-limited, with Stokes drift strongly attenuated beneath sea ice despite frequent wind forcing of OW magnitude. Favorable conditions for LT mixing are intermittent and largely confined to the MIZ, while the interior pack ice remains persistently shear-dominated. Mixing regimes showed clear spatial and temporal organization, with intermittent, event-driven transitions concentrated in the MIZ, superimposed on otherwise persistent seasonal states. We further demonstrate that SIC alone does not uniquely determine LT forcing, as local wave conditions and ice heterogeneity modulate the balance between shear- and wave-driven turbulence. Finally, we show that while wind–wave misalignment introduces substantial variability in diagnostic LT metrics, its impact on mixing remains small, indicating that LT efficiency is controlled primarily by the magnitude of wave forcing rather than its orientation. This work provides a coherent framework for interpreting the spatial and temporal structure of LT mixing potential across the Arctic, highlighting the following key findings.

430
435

4.1 The marginal ice zone as a dynamically distinct mixing regime

The MIZ emerges not simply as a geometric transition zone, but as a dynamically distinct mixing regime in which wave, wind, and ice processes interact to produce intermittent LT forcing. While conditions resembling open-water forcing occur primarily within the MIZ, LT activity is not controlled by MIZ extent alone. Instead, it is governed by the intensity and coherence of wind–wave forcing, which varies seasonally and episodically. As a result, periods of broad MIZ coverage do not necessarily correspond to enhanced LT activity, whereas dynamically active ice-edge regions can support strong, transient LT forcing. The mixing regime-based analysis further shows that LT variability is closely linked to threshold behavior between shear-, mixed-, and wave-dominated states. Regime instability peaks where grid cells frequently cross these physically defined boundaries, indicating that mixing variability arises from fluctuations in forcing that shift the balance between competing processes, rather than from large-scale ice extent alone. This highlights the MIZ as a region of enhanced variability and frequent reorganization of surface forcing, where LT emerges intermittently in response to episodic wave–ice interaction. This behavior extends earlier work showing that ice-edge variability is governed by dynamical thresholds rather than ice extent alone (Horvat et al., 2016).

4.2 Sea ice regulation of Stokes drift and Langmuir turbulence mixing potential

SIC provides a first-order constraint on the *mean* balance between wave- and shear-driven turbulence by regulating the attenuation of Stokes drift. For most seasons, median La_t increases with SIC, reflecting the progressive suppression of wave-driven forcing relative to wind stress as ice cover increases. This leads to predominantly shear-dominated conditions in the central Arctic. However, SIC alone does not fully explain the variability in LT forcing. Significant departures from the mean SIC– La_t relationship arise across seasons, indicating that additional processes modulate the realized balance between wave and shear forcing. In particular, reduced La_t at higher SIC during summer reflects intermittent wave penetration enabled by thinner, more fragmented ice and enhanced floe-scale heterogeneity. Under these conditions, long-period swell can episodically access nominally ice-covered regions, temporarily enhancing Stokes drift without establishing sustained wave-driven mixing. This indicates that SIC constrains the background forcing state but does not capture the processes that govern LT variability and intermittency.

4.3 Energetics and the role of misalignment

Energetic metrics show that variability in LT mixing is governed primarily by the intermittency of mechanical forcing rather than its mean magnitude. Highly intermittent dissipation is strongly localized to the same MIZ corridors that exhibit frequent regime transitions, indicating that episodic events, such as storms and transient wave penetration, dominate the temporal evolution of mixing. This behavior is consistent with previous studies showing that turbulent mixing in both open-ocean and ice-covered environments is controlled by intermittent, high-energy events rather than by time-mean forcing (Belcher et al., 2012; McWilliams, 2016; Arduin et al., 2016; Thomson, 2022; Boutin et al., 2022). Wind–wave misalignment introduces an additional geometric constraint on LT efficiency by reducing the effective projection of Stokes shear onto the Langmuir cell axis. While spatial diagnostics indicate substantial variability in projected LT metrics, the statistical analysis of misalignment

angles shows that near-aligned conditions dominate, with most angles below $\sim 30^\circ$, and larger misalignment occurring primarily in the MIZ. The energetic response to misalignment is weak. Hence, despite misalignment perturbing LT metrics, its effect on mixing is secondary, with typical changes in VKE remaining small relative to variability driven by wave forcing. LT energetics are controlled primarily by the magnitude and intermittency of wave forcing, while geometric effects act only as a weak modulation. In summary, LT in the Arctic is primarily controlled by intermittent wave forcing within the MIZ, with sea ice setting the background state and misalignment playing a secondary role.

475 **4.4 Implications for Arctic mixed layer dynamics and model development**

Our results show that LT in the Arctic is strongly constrained by wave–ice interactions. Wave attenuation beneath consolidated ice limits Stokes drift and confines wave-driven mixing primarily to the MIZ. Thus, parameterizations based on open-ocean conditions are likely to overestimate both the extent and persistence of Langmuir-driven mixing in ice-covered regions. LT forcing is also highly intermittent, driven by episodic wind–wave events along the evolving ice edge. Capturing this variability requires parameterizations that respond to changes in Stokes drift, rather than relying solely on bulk ice properties or steady forcing assumptions. In contrast, wind–wave misalignment plays a secondary role. Although it modifies diagnostic LT metrics, its effect on energetics is small relative to variability associated with wave forcing. These results suggest that improving the representation of wave attenuation and Stokes drift under sea ice is more important than explicitly resolving directional effects for modeling Arctic mixed-layer dynamics.

485 **4.5 Limitations and future directions**

Our approach is based on bulk diagnostics and empirically derived scalings and therefore carries several important limitations. The use of ~ 25 km resolution fields limits our ability to resolve fine-scale processes such as submesoscale eddies, floe-scale wave attenuation, and narrow leads and polynyas, all of which can locally modulate LT and upper-ocean mixing. While neighborhood-based statistics partially capture local heterogeneity, direct assessment of these processes requires higher-resolution modeling and targeted *in situ* observations. In addition, our analysis relies on a coupled sea ice–wave framework in which the ocean mixed layer does not respond dynamically to wind–wave forcing, and stratification feedbacks are not explicitly resolved. Mixed-layer depth and buoyancy effects are prescribed, limiting the realism of the diagnosed vertical mixing response. In particular, buoyancy-driven convection and LT are expected to interact nonlinearly in ice-covered and meltwater-influenced environments, yet their relative contributions remain poorly constrained. As a result, the metrics presented here should be interpreted as indicators of LT mixing *potential*, rather than predictions of realized turbulent states.

Addressing these challenges ultimately requires fully coupled ocean–wave–ice models that resolve stratification, wave propagation beneath ice, and wind–wave misalignment simultaneously. Recent and ongoing studies are beginning to resolve Langmuir turbulence under partially ice-covered and weakly stratified regimes using large-eddy simulations, regional modeling, and coordinated observations (e.g., Brenner et al., 2023; Lee et al., 2025). These efforts provide a clear pathway toward stratification-aware, ice-modified Langmuir parameterizations.

Complementary observational efforts are also essential. Coordinated field campaigns employing autonomous profilers, SWIFT drifters, and satellite altimetry will be critical for evaluating Langmuir diagnostics and parameterizations in ice-covered waters. In particular, observational and modeling studies should prioritize the MIZ, where wave–ice–wind interactions are most dynamically active. Finally, quantifying the impact of LT on vertical tracer transport, stratification erosion, and ice–ocean heat exchange in climate models will be essential for assessing its broader role in the evolving Arctic system.

4.6 Data Availability

The model outputs and post-processed Langmuir turbulence diagnostics used in this study are publicly available via Zenodo at <https://zenodo.org/records/17372007> and via the Arctic Data Center (urn:uuid:20106fcf-9bcf-4515-bb5c-cb54b2e61553). Analysis scripts are hosted on GitHub at https://github.com/atavri/Langmuir_turbulence_Arctic.git. ERA5 atmospheric reanalysis data are available from the Copernicus Climate Data Store, and the GLORYS12V1 ocean reanalysis is available through the Copernicus Marine Service.

4.7 Author contribution

A.T. led the study, including conceptualization, analysis, and writing of the original draft. C.H., B.P., and A.T. contributed to interpretation of results and manuscript review and editing. G.B. contributed to model data curation and technical support. A.H. and A.K. contributed to early analysis and scientific discussion.

4.8 Competing Interests

The authors declare that they have no competing interests.

4.9 Acknowledgements

This research was supported in part by the National Science Foundation (NSF OPP-2146910 and OCE-2148655) and by Schmidt Sciences, LLC through the SASIP project. The simulations were performed using resources provided by Sigma2-the National Infrastructure for High-Performance Computing and Data Storage in Norway and supported by the Research Council of Norway (project ForWARD, 345055). We thank Sam Brenner and Baylor Fox-Kemper for their insightful discussions that helped shape the use of the Langmuir turbulence parameterizations.

References

- 525 Ali, A., Christensen, K. H., Breivik, Ø., Malila, M., Raj, R. P., Bertino, L., Chassignet, E. P., and Bakhoday-Paskyabi, M.: A comparison of Langmuir turbulence parameterizations and key wave effects in a numerical model of the North Atlantic and Arctic Oceans, *Ocean Modelling*, 137, 76–97, 2019.
- Ardhuin, F., Sutherland, P., Doble, M., and Wadhams, P.: Ocean waves across the Arctic: Attenuation due to dissipation dominates over scattering for periods longer than 19 s, *Geophysical Research Letters*, 43, 5775–5783, 2016.
- 530 Ardhuin, F., Boutin, G., Stopa, J., Girard-Ardhuin, F., Melsheimer, C., Thomson, J., Kohout, A., Doble, M., and Wadhams, P.: Wave attenuation through an Arctic marginal ice zone on 12 October 2015: 2. Numerical modeling of waves and associated ice breakup, *Journal of Geophysical Research: Oceans*, 123, 5652–5668, 2018.
- Ardhuin, F., Otero, M., Merrifield, S., Grouazel, A., and Terrill, E.: Ice breakup controls dissipation of wind waves across southern ocean sea ice, *Geophysical Research Letters*, 47, e2020GL087699, 2020.
- 535 Armitage, T. W., Bacon, S., Ridout, A. L., Petty, A. A., Wolbach, S., and Tsamados, M.: Arctic Ocean surface geostrophic circulation 2003–2014, *The Cryosphere*, 11, 1767–1780, 2017.
- Belcher, S. E., Grant, A. L., Hanley, K. E., Fox-Kemper, B., Van Roekel, L., Sullivan, P. P., Large, W. G., Brown, A., Hines, A., Calvert, D., et al.: A global perspective on Langmuir turbulence in the ocean surface boundary layer, *Geophysical Research Letters*, 39, 2012.
- Boutin, G., Ardhuin, F., Dumont, D., Sévigny, C., Girard-Ardhuin, F., and Accensi, M.: Floe size effect on wave-ice interactions: Possible effects, implementation in wave model, and evaluation, *Journal of Geophysical Research: Oceans*, 123, 4779–4805, 2018.
- 540 Boutin, G., Lique, C., Ardhuin, F., Rousset, C., Talandier, C., Accensi, M., and Girard-Ardhuin, F.: Towards a coupled model to investigate wave–sea ice interactions in the Arctic marginal ice zone, *The Cryosphere*, 14, 709–735, 2020.
- Boutin, G., Williams, T., Rampal, P., Olason, E., and Lique, C.: Wave–sea-ice interactions in a brittle rheological framework, *Cryosphere*, 15, 431–457, 2021.
- 545 Boutin, G., Williams, T., Horvat, C., and Brodeau, L.: Modelling the Arctic wave-affected marginal ice zone: a comparison with ICESat-2 observations, *Philosophical Transactions of the Royal Society A*, 380, 20210262, 2022.
- Brenner, S. and Horvat, C.: Scaling simulations of local wind-waves amid sea ice floes, *Journal of Geophysical Research: Oceans*, 129, e2024JC021629, 2024.
- Brenner, S., Rainville, L., Thomson, J., Cole, S., and Lee, C.: Comparing observations and parameterizations of ice-ocean drag through an annual cycle across the Beaufort Sea, *Journal of Geophysical Research: Oceans*, 126, e2020JC016977, 2021.
- 550 Brenner, S., Horvat, C., Hall, P., Lo Piccolo, A., Fox-Kemper, B., Labbé, S., and Dansereau, V.: Scale-dependent air-sea exchange in the polar oceans: Floe-floe and floe-flow coupling in the generation of ice-ocean boundary layer turbulence, *Geophysical Research Letters*, 50, e2023GL105703, 2023.
- Collins, C., Doble, M., Lund, B., and Smith, M.: Observations of surface wave dispersion in the marginal ice zone, *Journal of Geophysical Research: Oceans*, 123, 3336–3354, 2018.
- 555 Cooper, V. T., Roach, L., Thomson, J., Brenner, S., Smith, M., Meylan, M., and Bitz, C.: Wind waves in sea ice of the western Arctic and a global coupled wave-ice model, *Philosophical Transactions of the Royal Society A*, 380, 20210258, 2022.
- Craik, A. D. and Leibovich, S.: A rational model for Langmuir circulations, *Journal of Fluid Mechanics*, 73, 401–426, 1976.
- D’Asaro, E. A.: Turbulence in the upper-ocean mixed layer, *Annual review of marine science*, 6, 101–115, 2014.

- 560 Dethleff, D. and Kempema, E.: Langmuir circulation driving sediment entrainment into newly formed ice: Tank experiment results with application to nature (Lake Hattie, United States; Kara Sea, Siberia), *Journal of Geophysical Research: Oceans*, 112, 2007.
- Dosser, H. V. and Rainville, L.: Dynamics of the changing near-inertial internal wave field in the Arctic Ocean, *Journal of Physical Oceanography*, 46, 395–415, 2016.
- Drucker, R., Martin, S., and Moritz, R.: Observations of ice thickness and frazil ice in the St. Lawrence Island polynya from satellite imagery, upward looking sonar, and salinity/temperature moorings, *Journal of Geophysical Research: Oceans*, 108, 2003.
- 565 Fan, Y. and Griffies, S. M.: Impacts of parameterized Langmuir turbulence and nonbreaking wave mixing in global climate simulations, *Journal of Climate*, 27, 4752–4775, 2014.
- Gargett, A. and Grosch, C.: Turbulence process domination under the combined forcings of wind stress, the Langmuir vortex force, and surface cooling, *Journal of Physical Oceanography*, 44, 44–67, 2014.
- 570 Harcourt, R. R.: An improved second-moment closure model of Langmuir turbulence, *Journal of Physical Oceanography*, 45, 84–103, 2015.
- Harcourt, R. R. and D’Asaro, E. A.: Large-eddy simulation of Langmuir turbulence in pure wind seas, *Journal of Physical Oceanography*, 38, 1542–1562, 2008.
- Herman, A.: Wave-induced stress and breaking of sea ice in a coupled hydrodynamic discrete-element wave–ice model, *The Cryosphere*, 11, 2711–2725, 2017.
- 575 Horvat, C., Tziperman, E., and Campin, J.-M.: Interaction of sea ice floe size, ocean eddies, and sea ice melting, *Geophysical Research Letters*, 43, 8083–8090, 2016.
- Horvat, C., Blanchard-Wrigglesworth, E., and Petty, A.: Observing waves in sea ice with ICESat-2, *Geophysical Research Letters*, 47, e2020GL087629, 2020.
- Kirillov, S. A., Dmitrenko, I. A., Hölemann, J. A., Kassens, H., and Bloshkina, E.: The penetrative mixing in the Laptev Sea coastal polynya pycnocline layer, *Continental Shelf Research*, 63, 34–42, 2013.
- 580 Kukulka, T., Plueddemann, A. J., Trowbridge, J. H., and Sullivan, P. P.: Rapid mixed layer deepening by the combination of Langmuir and shear instabilities: A case study, *Journal of Physical Oceanography*, 40, 2381–2400, 2010.
- Kukulka, T., Plueddemann, A. J., and Sullivan, P. P.: Inhibited upper ocean restratification in nonequilibrium swell conditions, *Geophysical Research Letters*, 40, 3672–3676, 2013.
- 585 Lee, A., Hutchings, J., Horvat, C., Tavri, A., and Pearson, B.: Impact of Surface Waves on Mixing and Circulation in a Summertime Lead, *EGUsphere*, 2025, 1–33, 2025.
- Leibovich, S.: The form and dynamics of Langmuir circulations, *Annual review of fluid mechanics*, 15, 391–427, 1983.
- Li, Q. and Fox-Kemper, B.: Assessing the effects of Langmuir turbulence on the entrainment buoyancy flux in the ocean surface boundary layer, *Journal of Physical Oceanography*, 47, 2863–2886, 2017.
- 590 Li, Q., Webb, A., Fox-Kemper, B., Craig, A., Danabasoglu, G., Large, W. G., and Vertenstein, M.: Langmuir mixing effects on global climate: WAVEWATCH III in CESM, *Ocean Modelling*, 103, 145–160, 2016.
- Li, Q., Fox-Kemper, B., Breivik, Ø., and Webb, A.: Statistical models of global Langmuir mixing, *Ocean Modelling*, 113, 95–114, 2017.
- Li, Q., Reichl, B. G., Fox-Kemper, B., Adcroft, A. J., Belcher, S. E., Danabasoglu, G., Grant, A. L., Griffies, S. M., Hallberg, R., Hara, T., et al.: Comparing ocean surface boundary vertical mixing schemes including Langmuir turbulence, *Journal of Advances in Modeling Earth Systems*, 11, 3545–3592, 2019.
- 595 Liu, A. K. and Mollo-Christensen, E.: Wave propagation in a solid ice pack, *Journal of physical oceanography*, 18, 1702–1712, 1988.

- Lo Piccolo, A., Horvat, C., and Fox-Kemper, B.: Energetics and Transfer of Submesoscale Brine-Driven Eddies at a Sea Ice Edge, *Journal of Physical Oceanography*, 54, 1489–1501, 2024.
- Manucharyan, G. E. and Thompson, A. F.: Submesoscale sea ice-ocean interactions in marginal ice zones, *Journal of Geophysical Research: Oceans*, 122, 9455–9475, 2017.
- 600
- McWilliams, J. C.: Submesoscale currents in the ocean, *Proceedings of the Royal Society A: Mathematical, Physical and Engineering Sciences*, 472, 20160 117, 2016.
- McWilliams, J. C., Sullivan, P. P., and Moeng, C.-H.: Langmuir turbulence in the ocean, *Journal of Fluid Mechanics*, 334, 1–30, 1997.
- Morison, J. H., Long, C. E., and Levine, M. D.: Internal wave dissipation under sea ice, *Journal of Geophysical Research: Oceans*, 90, 11 959–11 966, 1985.
- 605
- Muilwijk, M., Hattermann, T., Martin, T., and Granskog, M. A.: Future sea ice weakening amplifies wind-driven trends in surface stress and Arctic Ocean spin-up, *Nature Communications*, 15, 6889, 2024.
- Ólason, E., Boutin, G., Williams, T., Korosov, A., Regan, H., Rheinländer, J., Rampal, P., Flocco, D., Samaké, A., Davy, R., et al.: The next generation sea-ice model neXtSIM, version 2, *EGUphere*, 2025, 1–33, 2025.
- 610
- Pearson, B. C., Grant, A. L., Polton, J. A., and Belcher, S. E.: Langmuir turbulence and surface heating in the ocean surface boundary layer, *Journal of Physical Oceanography*, 45, 2897–2911, 2015.
- Pearson, B. C., Grant, A. L., and Polton, J. A.: Pressure–strain terms in Langmuir turbulence, *Journal of Fluid Mechanics*, 880, 5–31, 2019.
- Pinkel, R.: Near-inertial wave propagation in the western Arctic, *Journal of physical oceanography*, 35, 645–665, 2005.
- Polton, J. A. and Belcher, S. E.: Langmuir turbulence and deeply penetrating jets in an unstratified mixed layer, *Journal of Geophysical Research: Oceans*, 112, 2007.
- 615
- Rainville, L., Lee, C. M., and Woodgate, R. A.: Impact of wind-driven mixing in the Arctic Ocean, *Oceanography*, 24, 136–145, 2011.
- Rampal, P., Bouillon, S., Ólason, E., and Morlighem, M.: neXtSIM: a new Lagrangian sea ice model, *The Cryosphere*, 10, 1055–1073, 2016.
- Reichl, B. G. and Li, Q.: A parameterization with a constrained potential energy conversion rate of vertical mixing due to Langmuir turbulence, *Journal of Physical Oceanography*, 49, 2935–2959, 2019.
- 620
- Reichl, B. G., Wang, D., Hara, T., Ginis, I., and Kukulka, T.: Langmuir turbulence parameterization in tropical cyclone conditions, *Journal of Physical Oceanography*, 46, 863–886, 2016.
- Skyllingstad, E. D. and Denbo, D. W.: An ocean large-eddy simulation of Langmuir circulations and convection in the surface mixed layer, *Journal of Geophysical Research: Oceans*, 100, 8501–8522, 1995.
- Skyllingstad, E. D. and Denbo, D. W.: Turbulence beneath sea ice and leads: A coupled sea ice/large-eddy simulation study, *Journal of Geophysical Research: Oceans*, 106, 2477–2497, 2001.
- 625
- Squire, V. A.: A fresh look at how ocean waves and sea ice interact, *Philosophical Transactions of the Royal Society A: Mathematical, Physical and Engineering Sciences*, 376, 20170 342, 2018.
- Stopa, J. E., Ardhuin, F., and Girard-Ardhuin, F.: Wave climate in the Arctic 1992–2014: Seasonality and trends, *The Cryosphere*, 10, 1605–1629, 2016.
- 630
- Sullivan, P. P., McWILLIAMS, J. C., and Melville, W. K.: Surface gravity wave effects in the oceanic boundary layer: Large-eddy simulation with vortex force and stochastic breakers, *Journal of Fluid Mechanics*, 593, 405–452, 2007.
- Thomson, J.: Wave propagation in the marginal ice zone: connections and feedback mechanisms within the air–ice–ocean system, *Philosophical Transactions of the Royal Society A*, 380, 20210 251, 2022.
- Thomson, J. and Rogers, W. E.: Swell and sea in the emerging Arctic Ocean, *Geophysical Research Letters*, 41, 3136–3140, 2014.

- 635 Tolman, H. L. et al.: User manual and system documentation of WAVEWATCH III TM version 3.14, Technical note, MMAB contribution, 276, 2009.
- Van Roekel, L., Fox-Kemper, B., Sullivan, P., Hamlington, P., and Haney, S.: The form and orientation of Langmuir cells for misaligned winds and waves, *Journal of Geophysical Research: Oceans*, 117, 2012.
- Voermans, J., Babanin, A., Thomson, J., Smith, M., and Shen, H.: Wave attenuation by sea ice turbulence, *Geophysical Research Letters*, 46, 640 6796–6803, 2019.
- Webb, A. and Fox-Kemper, B.: Wave spectral moments and Stokes drift estimation, *Ocean modelling*, 40, 273–288, 2011.
- Yang, D., Chamecki, M., and Meneveau, C.: Inhibition of oil plume dilution in Langmuir ocean circulation, *Geophysical Research Letters*, 41, 1632–1638, 2014.